

Supplemental Information

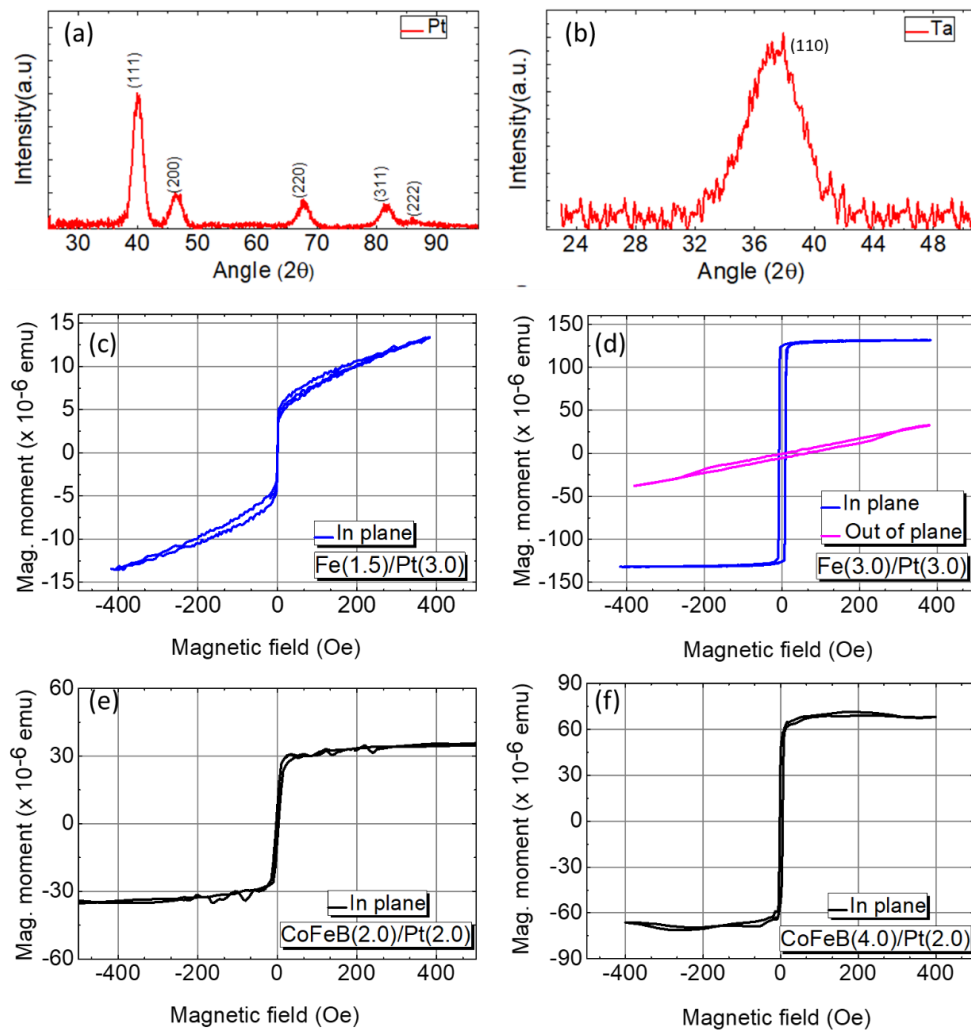


Figure S1 XRD plots of (a) Pt film, and (b) α -phase Ta film. The crystallographic planes corresponding to various XRD peaks have been marked. Hysteresis loops from in-plane and out-of-plane magnetic measurements using vibrating sample magnetometer on (c) Fe(1.5)/Pt(3.0), (d) Fe(3.0)/Pt(3.0), (e) CoFeB(2.0)/Pt(2.0), and (f) CoFeB(4.0)/Pt(2.0) bilayer FM/NM spintronic heterostructures. Related to **Star Method**.

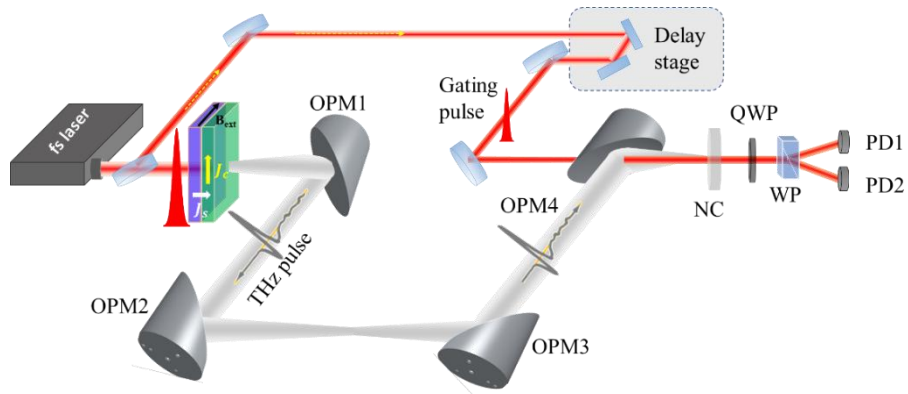


Figure S2.1 Configuration 1: Time-domain THz spectroscopy setup using spintronic emitters. Pulsed THz generation from the excitation of the spintronics heterostructures with femtosecond NIR pulse and probing of the THz pulses by electro-optic sampling in a nonlinear optical crystal. OPMs: off-axis parabolic mirrors, QWP: quarter-wave plate, NC: nonlinear optical crystal, WP: Wollaston prism, PD: photodiode, LIA: lock-in amplifier, B_{ext} : applied external magnetic field, J_s : spin current, J_c : charge current. Related to **Star Method**.

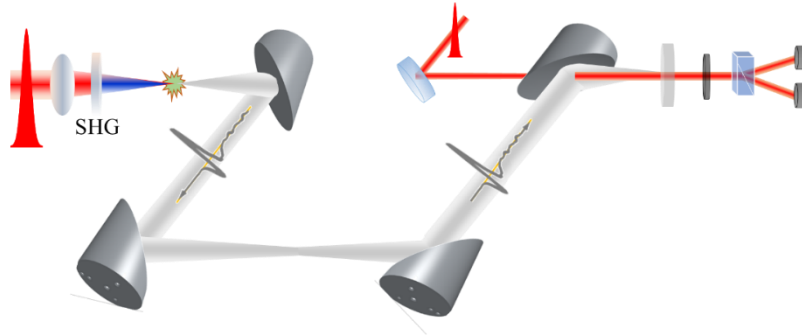


Figure S2.2 Configuration 2: Time-domain THz spectroscopy setup using dual-color air-plasma source. SHG: second harmonic generation crystal. Related to **Star Method**.

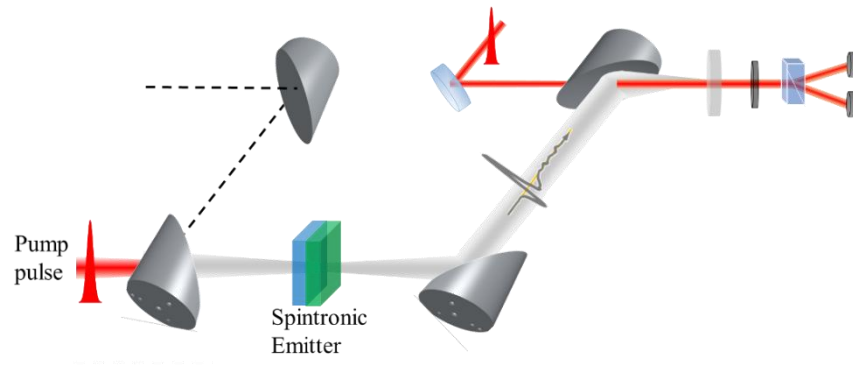


Figure S3 Configuration 3: Experimental setup for THz time-domain spectroscopy using spintronic emitters and to determine their optical damage threshold. Related to **Star Method**.

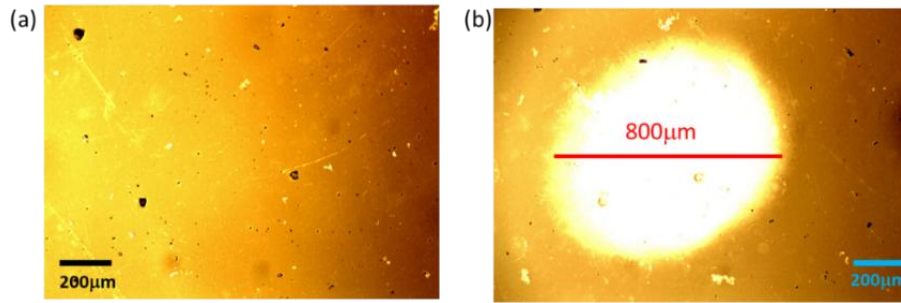


Figure S4.1. Optical microscopy images of the representative spintronic emitter taken in the transmission mode using a 10X objective lens. (a) before and (b) after the optical damage. Related to **Figure 7**.

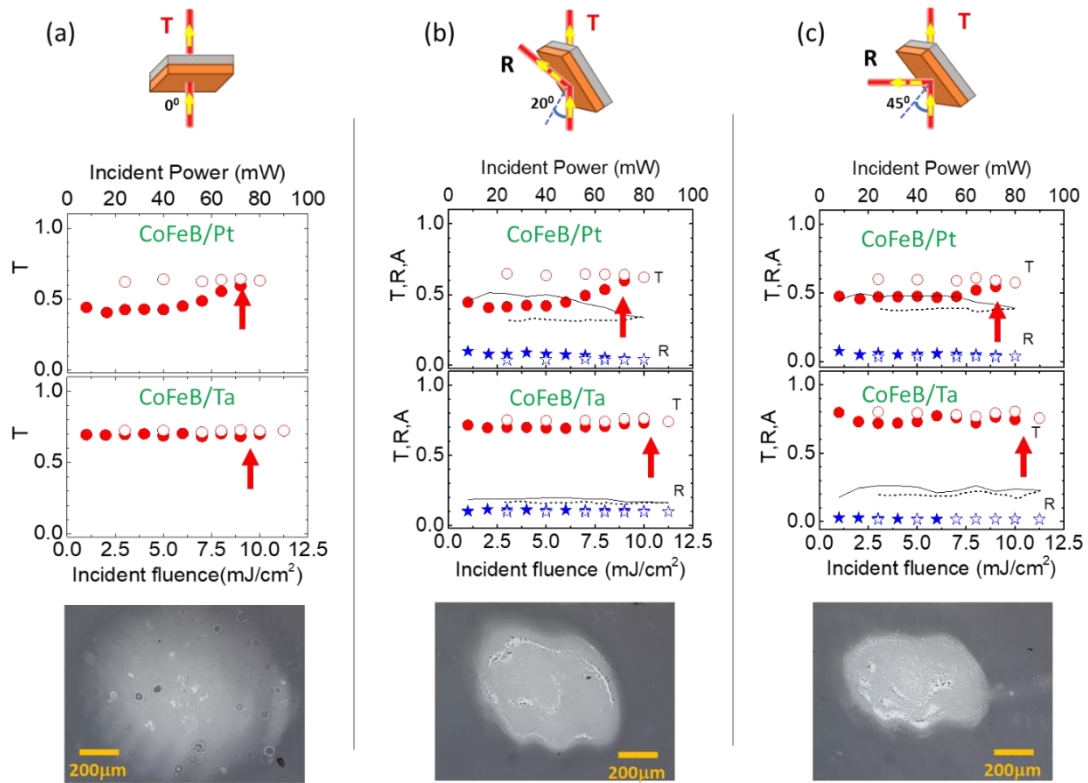


Figure S4.2 Optical transmittance (T) and reflectance (R) measurements with respect to the incident laser fluence (power) on the spintronic emitters at three different incident angles as indicated. The representative samples are CoFeB(3)/Pt(3) and CoFeB(3)/Ta(3), both on quartz substrates. Solid symbols are for increasing power while the open symbols are for lowering power values. The optical microscopy images were taken after the optical damage of the CoFeB/Pt sample at certain fluences (powers) indicated by vertically up arrows. There was hardly any damage to the CoFeB/Ta sample on the quartz substrate upto the highest experimental fluence. Thin continuous and dotted black lines in (b) and (c) are the absorbance values while increasing and decreasing the excitation fluence, respectively. Related to **Figure 8**.

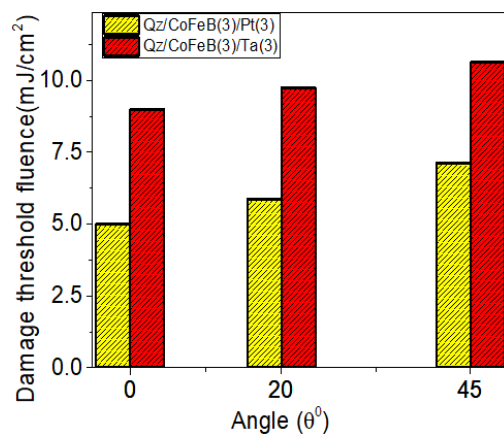


Figure S4.3 Angle of incidence dependent variation in the damage threshold fluence for CoFeB(3nm)/Pt(3nm) and CoFeB(3nm)/Ta(3nm) bilayer heterostructures on quartz substrate. Related to **Figure 8**.

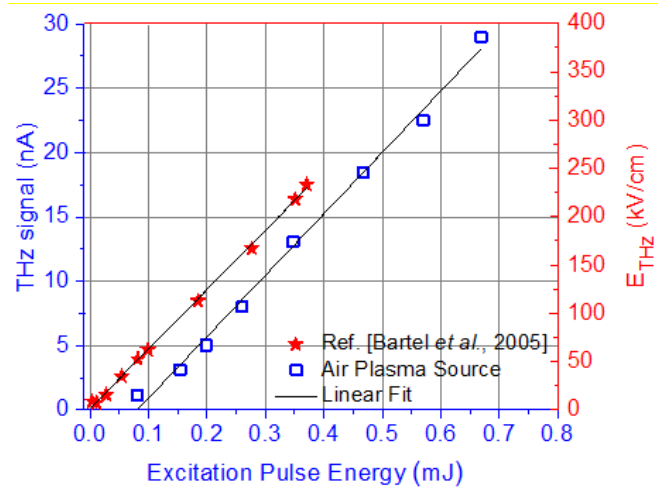


Figure S5 Comparison in THz signal generation from the coherent air-plasma source in our experiments and the literature [Bartel *et al.*, 2005]. At any given excitation pulse energy, the THz field is measured in nA in our experiments and in kV/cm in the literature [Bartel *et al.*, 2005]. The solid line represents the linear dependence of the THz field strength on the excitation pulse energy. Related to **Figure 6**.

S1. Structural and magnetic characterization of the samples

X-ray diffraction (XRD) and X-ray reflectivity (XRR) measurements were carried out using a PANalytical X'Pert diffractometer with a Cu-K_α source to determine the crystalline phase and purity of Pt and Ta thin films (Figure S1 (a) and (b)). In the case of Pt, various XRD peaks have been marked with the corresponding crystallographic planes and confirm the polycrystalline phase of the film that is consistent with the literature.(Pereira *et al.*, 2013) In the XRD pattern of Ta film, a broad diffusive peak centered at angle $2\theta = 38.0^\circ$ is due to the Bragg reflection from (110) planes and evidently shows the growth of Ta primarily in its α -phase. The same could not be done for the ferromagnetic thin films due to the limitation with the X-ray source and rapid oxidation problem with these uncapped films(Mos *et al.*, 2017). The crystalline α -phase of Ta is deliberately obtained by controlling the growth parameters during the deposition. The thickness and surface/interface roughness of the fabricated samples were found to be consistent with those expected from the optimized growth rate parameters in the deposition, which are confirmed from the XRR data fitted using the recursive theory by Parratt(Parratt, 1954). The surface and interfacial roughness is found to be less than ~ 0.6 nm for our samples.

Since the magnetization behavior of the ferromagnetic layer in the FM/NM structures, plays a crucial role in the generation of the THz radiation(Yang *et al.*, 2016), hence, the in-plane/out-of-plane magnetic hysteresis measurements were performed using vibrating sample magnetometer (VSM) of a physical property measurement system (PPMS from Quantum Design) as shown in Figure S1(c) to S1(f). The magnetic hysteresis loops are obtained from the in-plane and out-of-plane M-H measurements on Fe/Pt and in-plane for CoFeB/Pt bilayer heterostructures having fixed Pt layer thickness, but different thicknesses of the Fe and CoFeB layers. It can be seen from the Figure S1(c) and (d) that for Fe layer thickness of 1.5 nm, it shows a non-saturating type of behavior, whereas, for higher thickness, the sample shows a clear square hysteresis with the saturation magnetic field value of < 30 Oersted (Coercive field). The results for CoFeB/Pt show a saturating behavior for both the thicknesses of the CoFeB layer, while the corresponding coercive field value is ~ 20 Oe. The change in the nature of the M-H curve from nonsaturating to saturating, while increasing the Fe layer thickness from 1.5 nm to 3 nm, is because of the decrease in the relative contribution from the out-of-plane component of the magnetization. Clearly, for the 1.5 nm thickness, the magnetic easy-axis has a finite component in the out-of-plane, which vanishes above a critical thickness.(Allenspach and Bischof, 1992) Therefore, for Fe, the critical thickness is between 1.5 nm and 3 nm, an observation that is consistent with the previous reports.(Torosyan *et al.*, 2018) Our results clearly suggest the synthesis of high-quality thin films by RF magnetron sputtering.

In our THz generation measurements, the applied external in-plane magnetic field has been kept well above the saturation magnetization, i.e., $B_{\text{ext}} >$ coercive field value. It may be pointed out that the out-of-plane magnetic field is not important for our THz experiments as the charge current responsible for the generation of THz radiation is insensitive to the out-of-plane magnetization direction. Therefore, for all the comparative studies performed in our paper are for FM layer thicknesses such that the magnetic easy-axis lies in the plane, and for the external magnetic field lying in the surface/plane of the layer.

S2. THz time-domain spectroscopy setup

For testing the THz generation performance of our spintronic emitters, we developed a time-domain THz spectrometer (TDTS) that was pumped by ~ 35 femtosecond (fs) laser pulses centered at 800 nm from a Ti:sapphire regenerative amplifier operating at a 1 kHz pulse repetition rate. The optical layout of the TDTS is shown in Figure S2.1, S2.2, and S3 used in three different configurations. In configuration 1 (Figure S2.1), the spintronic emitters are used. The open setup is not purged with dry air/nitrogen, rather, all the experiments for our paper have been performed under normal humidity ($\sim 50\%$) at room temperature of the lab. The laser beam is divided into two-part in a 90:10 beam splitter: the stronger part (pulse energy ~ 0.35 mJ and beam diameter ~ 6 mm) is used to pump the THz emitter (spintronic heterostructure), while the weaker part (pulse energy ~ 0.4 μ J) was routed through a linear translational stage (for generating computer-controlled time-delays relative to the pump/excitation pulse) and used as the gating beam for the detection of the THz pulse on a nonlinear crystal. The diameter of the gating beam was kept at ~ 2 mm using an iris.

The collimated pump beam excites the spintronic emitter as shown in Figure S2.1. The excitation pulse energy or power is controlled by using a neutral density filter. THz radiation emanates from the extended point-like source in the spintronic structure in all possible directions, part of which is collected in the forward direction by using a 15 cm focal length 90° off-axis gold-coated parabolic mirror (OPM1). There are 3 more same-type OPMs used in our setup for giving flexibility to the setup for different experiments(Kumar *et al.*, 2021a; Kumar *et al.*, 2021b). After routing the THz beam through the four OPMs, it is focused onto a (110)-surface oriented 0.5 mm thick ZnTe crystal, where, it collinearly matches with the gating pulse in space and time. A high resistive silicon (HR-Si) wafer is placed just before OPM1 to avoid the residual 800 nm pump laser beam completely from reaching the other side of the setup. Commercial neodymium magnets were used to produce a uniform and static magnetic field (B_{ext}) of strength ~ 120 mT. Detection of the THz pulses takes place on the ZnTe crystal via electro-optic sampling of the gating pulse(Kumar *et al.*, 2021a; Kumar *et al.*, 2021b) and achieved using a

quarter-wave plate, Wollaston prism, a balanced photodiode, and lock-in amplifier. The pump beam was modulated at a frequency of 267 Hz by an optical chopper.

For a comparison between the THz generation efficiency of our spintronic emitters and the more standard technique based on a dual-color air plasma source, we reconfigured our TDTS setup for the later. The layout of the setup in this configuration (configuration 2) is shown in Figure S2.2. Of course, in this case, only the THz generation part is modified, while all other optical conditions with the pulse duration, optical alignment, and detection by electro-optic sampling are left unchanged. Therefore, while estimating the THz pulse energy/power from our air-plasma source by comparing it with the reported data in the literature for similar amplified laser pulse duration and pulse energies, any differences can be related to the optical conditioning in the two experiments. For the generation of intense THz pulses from our dual-color air-plasma source, we used a biconvex lens of focal length 15 cm to focus the fundamental and second harmonic beam in the air. Thus, generated white plasma creates forward propagating THz pulses if the fundamental and the second harmonic beams are mixed together properly by adjusting the orientation and crystal angle. We used a β -barium borate (BBO) type-I SHG crystal of thickness 100 μm for generating the second harmonic beam as shown in Figure S2.2. Thus, emitted THz radiation is collected by the OPM1 and then detected in the ZnTe crystal by electro-optic sampling as describe before. It may be noted from the 4f-geometry of the configurations I and II in Figs. S2.1 and S2.2 that the difference in the size of the THz source in the two (the optically excited region within the spintronic heterostructure and the air plasma, respectively) will result into a difference in the size of the THz beam on the nonlinear crystal for its detection. The optical gating beam size on the nonlinear crystal was kept the same at $\sim 2\text{mm}$. Therefore, it will amount to an underestimation of the actual THz power from the spintronic source, if no change in the position of the nonlinear crystal and other optical alignments are made in the setup.

S3. Optical excitation power-dependent measurements on spintronic THz emitters

For doing excitation power-dependent measurements on the spintronic heterostructures for evaluating their THz generation efficiency, we modified the setup to configuration 3 as shown in Figure S3. Here, the spintronic source is placed between the two inner parabolic mirrors and irradiated with a converging excitation beam allowed through the aperture in the second OPM. The diameter of the optical beam on the sample was $\sim 1\text{ mm}$. Like before, no change in the optical conditioning with all other things including the electro-optic detection, we made. Again, a HR-Si wafer was placed just after the emitter to avoid the residual pump from reaching the second part of the setup.

S4. The optical damage threshold of spintronic THz emitters

Figure S4.1 shows the optical microscopy images of a spintronic source before and after the optical damage. The images are taken in the transmission mode using a 10X objective lens. The sample for representation is Fe(2)/Pt(3) on quartz substrate and these experiments were conducted using the setup in its configuration 3 as described above. The size of the damage due to excessive heating at high-level optical excitation is close to the predetermined size of the excitation beam. The excitation power was continuously increased using a neutral density filter and at few values, the magnitude of the THz signal also was recorded, before a sudden decrease in the signal was observed due to the optical damage. Experiments on various samples on different substrates were conducted for evaluating the performance of spintronic THz emitters with the highest THz generation performance and highest optical damage threshold.

Figure S4.2 presents the experimentally measured optical transmittance (T) and reflectance (R) values with respect to the incident laser fluence (power) on the spintronic emitters at three different incident angles as indicated. From the amount of reflected and transmitted intensities with respect to the incident intensity, the substrate corrected values of the R and T were determined. The representative samples measured here are CoFeB(3)/Pt(3) and CoFeB(3)/Ta(3), both on quartz substrates. Solid symbols are for increasing the fluences while the open symbols are for lowering the fluences. The optical microscopy images were taken after the optical damage of the CoFeB/Pt sample at certain fluences (powers) indicated by vertically up arrows. There was a very weak damage to the CoFeB/Ta sample on the quartz substrate upto the highest experimental fluence. Thin continuous and dotted black lines in Figures S4.2(b) and S4.2(c) are the absorptance ($A = 1 - R - T$) values while increasing and decreasing the excitation fluences, respectively. Figure S4.3 shows the incident angle-dependent optical damage threshold values for the above two representative spintronic THz emitters. The transmittance (absorptance) of CoFeB(3)/Pt(3) is smaller (higher) than that of the CoFeB(3)/Ta(3). Obviously, for the excitation wavelength of 800 nm, the lower value of absorptance of CoFeB(3)/Ta(3) than CoFeB(3)/Pt(3) is consistent with the higher damage threshold for the prior, as shown in Figure S4.3.

S5. Estimation of the THz electric field

For estimating the absolute value of the THz electric field in V/cm, we compared the THz signal value of our coherent air-plasma source with that from the literature(Bartel *et al.*, 2005) having nearly the same experimental

conditions. At various excitation pulse energies, the signal due to THz electric field has been measured in the lock-in units of nA in our experiments. The same in the literature has been reported in terms of kV/cm. This comparison has been presented in Figure S5, where, a one-to-one correspondence between the two can be clearly seen. The data in the figure demonstrates a linear dependence of the THz field strength on the excitation pulse energy, while a small difference in the y-axis intercept is to do with the difference in the optical arrangement and the electro-optic detection in the two cases. From these results, it can be concluded that at any excitation pulse energy, an original value in 1 nA corresponds to ~17 kV/cm of THz electric field. This unit conversion has been used uniformly while comparing the results from different THz sources in Figure 6 of the main manuscript.

Supplemental references

Allenspach R and Bischof A 1992 Magnetization direction switching in Fe/Cu(100) epitaxial films: Temperature and thickness dependence *Physical Review Letters* **69** 3385-8

Bartel T, Gaal P, Reimann K, Woerner M and Elsaesser T 2005 Generation of single-cycle THz transients with high electric-field amplitudes *Opt. Lett.* **30** 2805-7

Kumar S, Singh A, Kumar S, Nivedan A, Tondusson M, Degert J, Oberlé J, Yun S J, Lee Y H and Freysz E 2021a Enhancement in optically induced ultrafast THz response of MoSe₂MoS₂ heterobilayer *Opt. Express* **29** 4181-90

Kumar S, Singh A, Nivedan A, Kumar S, Yun S J, Lee Y H, Tondusson M, Degert J, Oberle J and Freysz E 2021b Sub-bandgap activated charges transfer in a graphene-MoS₂-graphene heterostructure *Nano Select* **1**

Mos Y, Vermeulen A, Buisman C and Weijma J 2017 X-Ray Diffraction of Iron Containing Samples: The Importance of a Suitable Configuration *Solid State Phenomena* **262** 545-8

Parratt L G 1954 Surface Studies of Solids by Total Reflection of X-Rays *Physical Review* **95** 359-69

Pereira R, Marchesi L F, Freitas R G, Matos R and Pereira E C 2013 A low-cost platinum film deposited direct on glass substrate for electrochemical counter electrodes *Journal of Power Sources* **232** 254-7

Torosyan G, Keller S, Scheuer L, Beigang R and Papaioannou E T 2018 Optimized Spintronic Terahertz Emitters Based on Epitaxial Grown Fe/Pt Layer Structures *Scientific Reports* **8** 1311

Yang D, Liang J, Zhou C, Sun L, Zheng R, Luo S, Wu Y and Qi J 2016 Powerful and Tunable THz Emitters Based on the Fe/Pt Magnetic Heterostructure *Advanced Optical Materials* **4** 1944-9